PT Symmetry Breaking and Nonlinear Optical Isolation in Coupled Microcavities

Xin Zhou[1] and Y. D. Chong[1,2,*]

[1]*Division of Physics and Applied Physics,*

School of Physical and Mathematical Sciences,

Nanyang Technological University, Singapore 637371, Singapore

[2]*Centre for Disruptive Photonic Technologies,*

Nanyang Technological University, Singapore 637371, Singapore

Abstract

We perform a theoretical study of nonlinear optical isolator devices based on coupled microcavities with gain and loss. Using coupled-mode theory, we derive a correspondence between the boundary of asymptotic stability in the nonlinear regime, where gain saturation is present, and the PT-breaking transition in the underlying linear system. For zero detuning and weak input intensity, the onset of optical isolation can be rigorously derived, and corresponds precisely to the PT transition point. When the couplings to the external ports are unequal, the isolation ratio exhibits an abrupt jump at the transition point, determined by the ratio of the couplings. This could be exploited to realize an actively controlled nonlinear optical isolator, in which strong optical isolation can be switched on or off using tiny variations in the inter-resonator separation.

---
[*] yidong@ntu.edu.sg

I.   INTRODUCTION

For many years, the implementation of compact optical isolators has been a major research goal in the field of integrated optics [1, 2]. Optical isolation requires the breaking of Lorentz reciprocity; this is traditionally achieved using magneto-optic materials, but such materials are challenging to incorporate into integrated optics devices [3, 4]. The most commonly-pursued alternative method for breaking reciprocity is to exploit optical nonlinearity [1, 5–10]. Two recent demonstrations of nonlinearity-based on-chip optical isolators have drawn especially strong attention [9, 10]. These very similar experiments both featured a pair of coupled whispering-gallery microcavities, one containing loss and the other saturable (nonlinear) gain. Light transmission across the structure was found to be strongly nonreciprocal, depending on whether it first passed through the gain or loss resonator. Aided by the high Q factors of the resonators, isolation was observed for record-low powers of $\sim 1\mu\text{W}$ [9].

The use of dual resonators containing gain and loss in Refs. [9, 10] was inspired by "PT symmetric optics", which concerns optical structures that are invariant under simultaneous parity-flip (P) and time-reversal (T) operations [11–17, 19, 20]. The concept originated from the observation that PT symmetric Hamiltonians, despite being non-Hermitian, can exhibit real eigenvalue spectra [21, 22], as well as "PT-breaking transitions" between real and complex eigenvalue regimes. The PT-breaking transition point is an "exceptional point", where two eigenstates coalesce and the effective Hamiltonian becomes defective [23, 24]. Near the transition, the dynamical behavior of the optical fields can exhibit highly interesting features [25–27]; for instance, the presence of gain saturation has been found to stabilize PT-symmetric steady states past the usual PT transition point [26, 27].

Despite these intriguing conceptual links, it was not clear from Refs. [9, 10] how PT symmetry relates to the working of the nonlinear optical isolators in question. Strictly speaking, PT symmetry holds in the dual-resonator structures only in the linear limit; in the nonlinear regime, the gain saturates and no longer matches the loss, so the structures are not PT symmetric and do not possess distinct "PT-symmetric" or "PT-broken" phases. Ref. [9] indicated that optical isolation occurs (in the nonlinear regime) if the system is tuned so that it would be PT-broken *in the linear regime*; however, the actual correspondence was not shown theoretically nor experimentally. The dynamical behavior of the system, including

the uniqueness and stability of the steady-state solution(s), was also unexplored.

In this paper, we present a theoretical analysis of the dual-resonator structure, aiming to clarify the relationships between the PT phase, the performance of the nonlinear optical isolator, and the uniqueness and stability of the steady-state optical modes. Using coupled-mode theory [28–31], we study the conditions for steady-state solutions to exist, and the asymptotic stability of those solution(s). We find that stability in the nonlinear system has a close correspondence with the PT transition boundary of the underlying linear system. It is particularly useful to focus on the "weak-input limit", where the input intensity is low relative to the gain saturation threshold within the amplifying resonator. In this limit, we show that the nonlinear solutions at non-zero frequency detunings are asymptotically stable in the PT-symmetric phase, and become unstable in the PT-broken phase. For small frequency detunings, there can exist regions in the PT-broken phase where multiple steady-state solutions exist, and we show that only the highest-intensity solution is asymptotically stable. Specifically, there is always one stable steady-state solution at zero detuning.

For the zero-detuning case in the weak-input limit, we show that the *nonlinear* system exhibits a sharp transition between isolating behavior (corresponding to the PT-broken phase) and reciprocal behavior (corresponding to the PT-symmetric phase). Although this transition coincides exactly with the PT transition point, it is an inherently nonlinear effect, arising from a jump between different solution branches of the cubic equations governing the output intensities for forward and backward transmission.

We also show that the performance of the nonlinear optical isolator is modified in a useful way when the two resonator-to-waveguide coupling rates are unequal. In this case, a small shift across the transition point causes the isolation ratio (the ratio between forward and backward transmission intensities) to undergo an abrupt jump, which approaches a discontinuity in the weak-input limit. The magnitude of this jump is given by the ratio of the coupling rates. This phenomenon can be used to realize a nonlinear optical isolator that exhibits very large changes in the isolation ratio, actively controlled by tiny shifts in (e.g.) the inter-resonator separation.

II. COUPLED-MODE EQUATIONS

The dual-resonator structure is shown schematically in Fig. 1(a). The setup is identical to Refs. [9, 10], consisting of two evanescently coupled microcavities with resonant frequencies ω_1 and ω_2. One resonator contains saturable gain, and the other is lossy. The resonators are coupled to separate optical fiber waveguides, which act as input/output ports (labeled 1–4), with couplings κ_1 and κ_2. The direct inter-resonator coupling rate is μ. In the "forward transmission" configuration, light is injected from port 1 at a fixed operating frequency ω, exiting at ports 2 and 4. Alternatively, in the "backward transmission" configuration, light is injected at port 4 and exit at ports 1 and 3. We are interested in the level of isolation between ports 1 and 4, which serve as the operational input and output ports for the device.

The dual-resonator system can be described by coupled-mode equations [9, 10], formulated using the standard framework of coupled-mode theory [28–31]. In this section and the next, we briefly summarize these equations, which have previously been presented in Refs. [9, 10]. For forward transmission, the coupled-mode equations are

$$\frac{da_1}{dt} = (i\Delta\omega_1 + g)a_1 - i\mu a_2 \tag{1}$$

$$\frac{da_2}{dt} = (i\Delta\omega_2 - \gamma)a_2 - i\mu a_1 + \sqrt{\kappa_2}s_{\text{in}} \tag{2}$$

$$I_F = \kappa_1|a_1|^2. \tag{3}$$

Here, a_1 and a_2 denote the complex amplitudes for the slowly-varying field amplitudes in the gain resonator and loss resonators, respectively; $\Delta\omega_{1,2} \equiv \omega - \omega_{1,2}$ denote the operating frequency's detuning from each resonator's natural frequency; $g > 0$ and $\gamma > 0$ are the net gain rate in resonator 1 and the net loss rate in resonator 2; s_{in} is the amplitude of the incoming light in port 1; and I_F is the power transmitted forward into port 4.

For backward transmission, a different set of coupled-mode equations holds:

$$\frac{da_1}{dt} = (i\Delta\omega_1 + g)a_1 - i\mu a_2 + \sqrt{\kappa_1}\,s_{\text{in}} \tag{4}$$

$$\frac{da_2}{dt} = (i\Delta\omega_2 - \gamma)a_2 - i\mu a_1 \tag{5}$$

$$I_B = \kappa_2\,|a_2|^2, \tag{6}$$

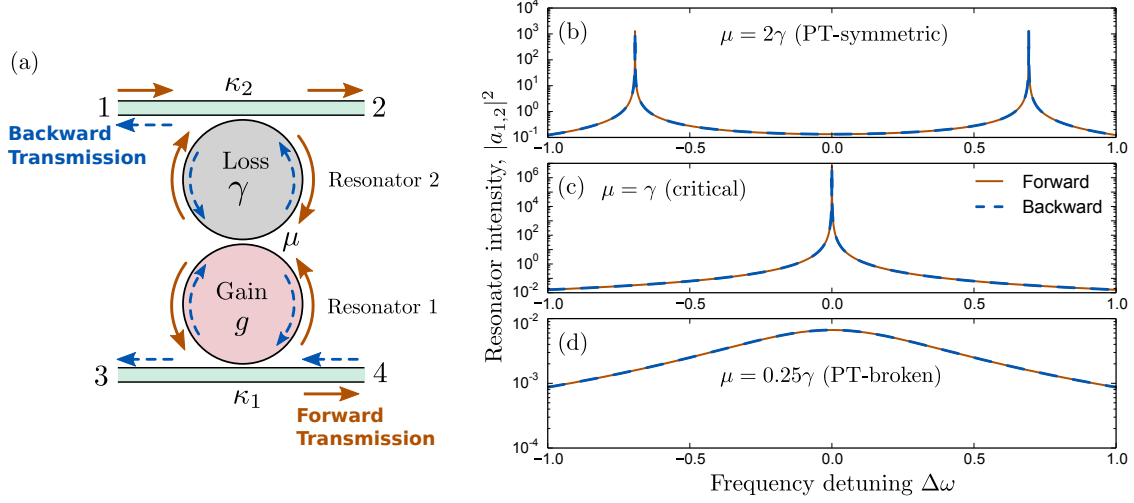where I_B is the power transmitted into port 1.

FIG. 1. (a) Schematic of a resonator with saturable gain coupled to a lossy resonator, with both resonators coupled to optical fiber ports. Solid arrows indicate forward transmission (port $1 \to 4$), and dashed arrows indicate backward transmission (port $4 \to 1$). (b)–(d) Transmission characteristics in the linear (non-gain-saturated) regime, when the gain and loss are PT symmetric ($g = \gamma = 0.4$). Here, we plot the intensity in the active resonator ($|a_1|^2$) under forward transmission (solid lines), and in the passive resonator ($|a_2|^2$) under backward transmission (dashes), versus the frequency detuning. These resonator intensities are proportional to the forward and backward transmission intensities via Eqs. (3) and (6). In the PT-symmetric phase $\mu > \gamma$, there are two transmission peaks; in the PT-broken phase $\mu < \gamma$, these merge into a single peak.

The gain/loss rates g and γ consist of several radiative and non-radiative terms [9]:

$$g = \frac{1}{2} \left(g' - \gamma_1 - \kappa_1 \right) \tag{7}$$

$$\gamma = \frac{1}{2} \left(\gamma_2 + \kappa_2 \right), \tag{8}$$

where g' is the intrinsic amplification rate in resonator 1, and $\gamma_{1,2}$ are the intrinsic loss rates in the resonators. Until stated otherwise, we will impose the following simplifying restrictions:

$$\kappa_1 = \kappa_2 = \gamma_1 = \gamma_2, \tag{9}$$

$$\Delta\omega_1 = \Delta\omega_2 \equiv \Delta\omega, \tag{10}$$

$$g' = \frac{g_0}{1 + |a_1/a_s|^2}. \tag{11}$$

5

Eq. (9) corresponds to a "critical coupling" criterion with respect to the individual cavity-waveguide couplings. The intrinsic loss and outcoupling rates are all tuned to the same value; note also that $g = g'/2 - \gamma$. Eq. (10) states that the resonators have the same natural frequency. Eqs. (9)–(10) serve as simplifying assumptions, to avoid dealing with a proliferation of free parameters; later, we will discuss the implications of relaxing these assumptions. Another important constraint, PT symmetry, will be imposed in the next section. Eq. (11) describes saturable gain, where g_0 is the unsaturated amplification rate, and $a_s \in \mathbb{R}^+$ is a gain saturation threshold.

The suitability of the system as an optical isolator is characterized using the "isolation ratio", which is the ratio of forward to backward transmittance at fixed input power:

$$R \equiv \frac{T_F}{T_B} = \frac{I_F(I_{\text{in}})}{I_B(I_{\text{in}})}, \tag{12}$$

where I_F is obtained by solving Eqs. (1)–(3) with $\dot{a}_1 = \dot{a}_2 = 0$ (steady state), and I_B is obtained from Eqs. (4)–(6). When the system is reciprocal, $R = 1$.

III. LINEAR OPERATION

We now impose the important constraint $g = \gamma$. This means that in the linear regime, $a_s \to \infty$, the gain and loss resonators become PT symmetric. To understand the implications, consider the "closed" system without resonator-fiber couplings. Its detuning eigenfrequencies are

$$\Delta\omega = i\frac{g - \gamma}{2} \pm \sqrt{\mu^2 - \gamma g - \left(\frac{g - \gamma}{2}\right)^2}. \tag{13}$$

When $g = \gamma$, these reduce to $\Delta\omega = \pm\sqrt{\mu^2 - \gamma^2}$. As μ and γ are varied while keeping $g = \gamma$, the system has a PT symmetry-breaking transition at $\mu = \gamma$. For $\mu > \gamma$, the detunings are real (PT-symmetric phase), and for $\mu < \gamma$ they are purely imaginary (PT-broken phase).

With the resonator-fiber couplings, the closed system's eigenmodes become transmission resonances. In the PT-symmetric phase $\mu > \gamma$, the resonator modes and transmission amplitudes exhibit two intensity peaks, at $\Delta\omega = \pm\sqrt{\mu^2 - \gamma^2}$, corresponding to the (real) detunings of the closed system, as shown in Fig. 1(b). In the PT-broken phase $\mu < \gamma$, there is a single peak at zero detuning, as shown in Fig. 1(d). As noted in Ref. [9], however, the

PT-symmetric and PT-broken phases will give very different isolation behaviors when gain saturation is introduced.

In the linear regime, the coupled-mode equations (1)–(3) and (4)–(6) obey optical reciprocity by explicit construction [29]. For fixed s_{in}, the forward and backward transmission amplitudes are exactly equal, $I_F = I_B$; the isolation ratio is $R = 1$, as shown in Fig. 1(b)–(d).

IV. NONLINEAR OPERATION: MULTIPLE SOLUTIONS AND STABILITY

We turn now to the nonlinear, gain-saturated regime, setting $g_0 = 4\gamma$, so that $g \to \gamma$ as $a_s \to \infty$. This means that the system would be PT symmetric in the absence of gain saturation. If we use a_s as the natural intensity scale for the coupled-mode equations, the nonlinear system has four remaining independent parameters: $\Delta\omega$, μ, γ, and $|s_{\text{in}}|^2$.

For finite a_s, optical reciprocity is broken, and the system can act as an isolator. However, it is no longer PT symmetric, since $g \neq \gamma$, and thus we can no longer rigorously define "PT symmetric" or "PT broken" phases. Still, we can relate the nonlinear system's isolation behavior to the PT symmetric phases *as defined in the linear limit*.

In the linear regime, the solutions to the coupled-mode equations were unique. With nonlinearity, the coupled-mode equations can have multiple steady-state solutions. For forward transmission, steady-state solutions are determined by combining Eqs. (1)–(2) into:

$$|\alpha|^2 x^3 + \left(2|\alpha - 1|^2 - 2 - \beta\right)x^2 + \left(|\alpha - 2|^2 - 2\beta\right)x - \beta = 0, \tag{14}$$

where α, β, and x are the following dimensionless variables:

$$\alpha = \frac{(-i\Delta\omega + \gamma)^2 + \mu^2}{\gamma(-i\Delta\omega + \gamma)}, \quad \beta = \frac{\mu^2}{\Delta\omega^2 + \gamma^2}\frac{1}{\gamma}\left|\frac{s_{\text{in}}}{a_s}\right|^2, \quad x = \left|\frac{a_1}{a_s}\right|^2. \tag{15}$$

Since $x \in \mathbb{R}^+$, there is either one, two, or three physical steady-state solutions. There must be at least one solution, since the polynomial has a positive third-order coefficient and negative zeroth-order coefficient. The backward transmission case is handled similarly, using Eqs. (4)–(5); it gives the same cubic equation (14), but with the replacement

$$\beta = \frac{1}{\gamma}\left|\frac{s_{\text{in}}}{a_s}\right|^2. \tag{16}$$

Solving the polynomial reveals a domain in parameter space where there are three physical steady-state solutions, outside of which the solution is unique. This is shown in Fig. 2(a)–
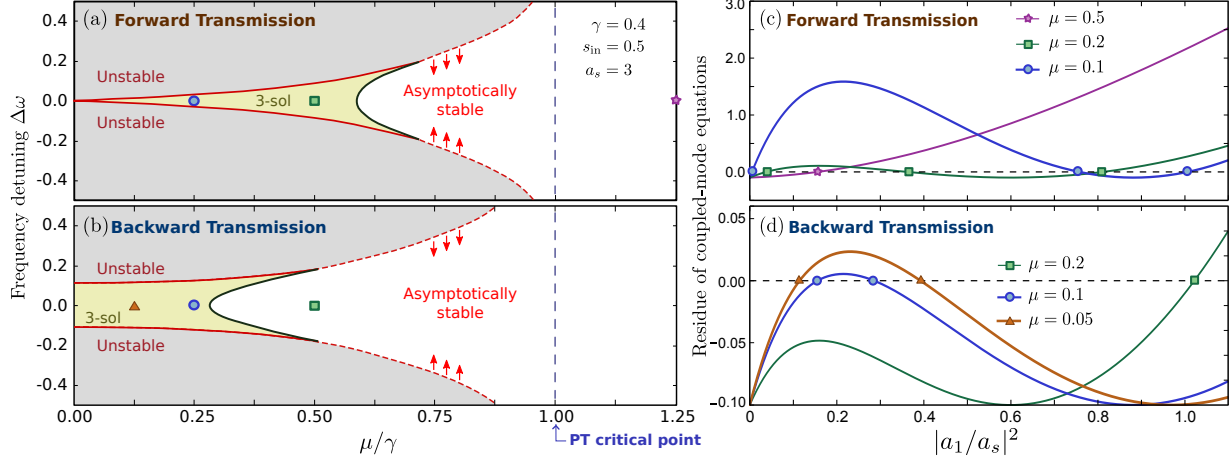
7

FIG. 2. (a)–(b) Domains in which the nonlinear coupled-mode equations have multiple steady-state solutions, for forward (a) and backward (b) transmission. Here, we show the parameter space defined by $\Delta\omega$ and μ, with fixed $\gamma = 0.4$, $s_{\text{in}} = 0.5$, and $a_s = 3$; symbols indicate the points in the parameter space corresponding to the curves in (c) and (d). Within the small-$\Delta\omega$ region bounded by the red curves, the highest-intensity (or only) solution is asymptotically stable. (c)–(d) Plots showing the emergence of multiple solutions at several values of μ, fixing $\Delta\omega = 0$. The horizontal axis is the normalized intensity in the gain resonator, $|a_1/a_s|^2$; the vertical axis is the left-hand side of the cubic Eq. (14), and its counterpart for backward transmission; the steady-state coupled-mode equations are satisfied when the curves cross zero.

(b). The three-solution domain lies within the "PT-broken" phase of the linear system, $\mu < \gamma$.

The boundaries of the three-solution domain depend on γ and s_{in}, as the choice of forward or backward transmission. It consists of two sets of curves; the black curves in Fig. 2(a)–(b) involve a degeneracy of two low-intensity roots of the cubic polynomial [Fig. 2(c)–(d)]. Crossing this boundary causes no discontinuity in the intensity of the stable steady-state solution. The red curves in Fig. 2(a)–(b) involve the degeneracy of two high-intensity roots of the cubic polynomial (14); as we shall see, crossing this boundary destabilizes the steady-state solution.

Through numerical stability analysis, detailed in Appendix A, we find that the highest-intensity solution in the three-solution domain is asymptotically stable (i.e., the Lyapunov exponents are all negative). The two lower-intensity solutions are *unstable*: small perturbations from these steady states eventually evolve into the highest-intensity state. In the

8

one-solution domain, the solution is asymptotically stable for small detuning $\Delta\omega$, and unstable for large $\Delta\omega$.

Interestingly, the region of asymptotic stability in the nonlinear system is closely connected to the PT symmetry phases of the linear system. For $\mu < \gamma$, which corresponds to the PT-broken phase, the frequency range of asymptotic stability is bounded by the solid and dashed red curves shown in Fig. 2(a)–(b). These bounds diverge at $\mu = \gamma$, which corresponds to the transition from the PT-broken to the PT-symmetric phase in the linear system. For $\mu > \gamma$, the steady state solution becomes asymptotically stable for all $\Delta\omega$.

In the one-solution domain, the onset of asymptotic instability (at sufficiently large $\Delta\omega$) is associated with the appearance of sustained time-domain beating in both the resonator intensities and the transmittance. This is shown in Appendix A (Fig. 6).

V. ISOLATION RATIOS AT ZERO DETUNING

Let us now focus on zero detuning, $\Delta\omega = 0$. In this case, there is always an asymptotically stable steady-state solution, and we shall be able to derive an important connection to the PT transition of the linear system. The variables α and β, defined in Eq. (15), simplify to

$$
\begin{aligned}
\alpha &= 1 + \left(\frac{\mu}{\gamma}\right)^2 \\
\beta &= \frac{|s_{\text{in}}/a_s|^2}{\gamma} \times \begin{cases} \left(\dfrac{\mu}{\gamma}\right)^2, & \text{(Forward)} \\ 1, & \text{(Backward)}. \end{cases}
\end{aligned}
\tag{17}
$$

Hence, the cubic polynomial in Eq. (14) is entirely determined by two quantities: (i) μ/γ and (ii) $|s_{\text{in}}/a_s|^2/\gamma$. The first quantity is also the tuning parameter for the PT transition. The second quantity determines the strength of the input relative to the gain saturation threshold. We will be particularly interested in the "weak-input" limit, defined as

$$
s_{\text{in}} \ll \sqrt{\gamma}\, a_s.
\tag{18}
$$

When $\beta \ll 1$, the steady state behavior will be principally determined by the PT-tuning parameter μ/γ.

Fig. 3 plots the isolation ratio $R \equiv I_F/I_B$ versus μ/γ, for several different values of γ and s_{in}. In the weak-input regime, the isolation ratio curves are almost identical for different
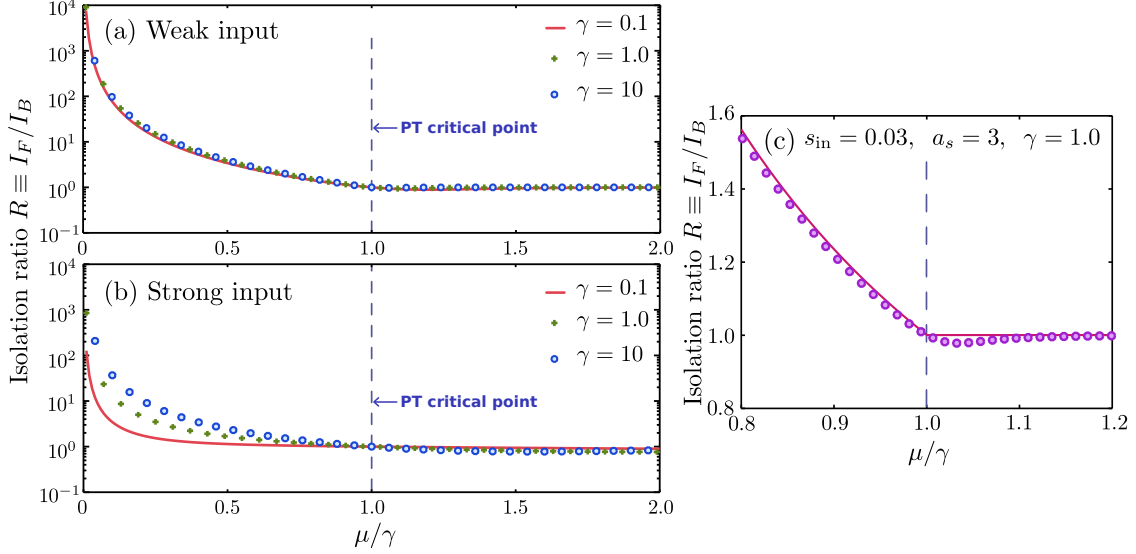
9

FIG. 3. Isolation ratio versus μ/γ, for (a) weak inputs $s_{\mathrm{in}} = 0.15$ and $a_s = 3$, and (b) strong inputs regime $s_{\mathrm{in}} = 9$ and $a_s = 3$, using several choices of γ. In the weak-input regime, the isolation ratio is mainly determined by the PT-breaking parameter μ/γ, and reaches a plateau for $\mu/\gamma > 1$, corresponding to the PT-symmetric phase of the linear system. (c) Isolation ratios near the $\mu/\gamma \approx 1$, showing the emergence of a "kink" in the weak-input regime. Circles show exact numerical solutions of the coupled-mode equations, and the solid curve shows the low-intensity limiting expressions given in Eqs. (21)–(22).

γ, which verifies that the system is controlled by the combination μ/γ. For $\mu/\gamma < 1$, corresponding to the PT-broken phase of the linear system, we find that $R > 1$, and hence the system functions as a good optical isolator. For $\mu/\gamma > 1$, we find that $R \approx 1$. This agrees with the qualitative behaviors reported in Ref. [9].

Let us examine the vicinity of the transition point in greater detail. Fig. 3(c) shows that in the weak input regime, the isolation ratio curve exhibits a kink at $\mu/\gamma = 1$. To understand this, we return to the definition of the isolation ratio:

$$R = \frac{I_F}{I_B} = (\mu/\gamma)^{-2}\, \frac{x_F}{x_B}, \tag{19}$$

where x_F and x_B are the solutions to Eq. (14) for the forward and backward transmission cases. For $\beta \to 0$, Eq. (14) reduces to

$$x\left(x - \frac{1 - (\mu/\gamma)^2}{1 + (\mu/\gamma)^2}\right)^2 = 0. \tag{20}$$

For $\mu/\gamma < 1$, the double-root in Eq. (20) is positive, and β is just a small correction. Hence, $x \approx 1$ to lowest order for forward and backward transmission, and Eq. (19) implies that

$$R \approx (\mu/\gamma)^{-2} \quad \text{for} \ \ \mu/\gamma < 1, \ \ s_{\text{in}} \ll \sqrt{\gamma} \, a_s. \tag{21}$$

For $\mu/\gamma > 1$, the double-root is negative, so the highest-intensity root in the $\beta \to 0$ limit is $x = 0$. For non-zero β, this root becomes $\mathcal{O}(\beta)$, so $x_F/x_B \approx \beta_F/\beta_B = (\mu/\gamma)^2$. The isolation ratio is

$$R \approx 1 \qquad \text{for} \ \ \mu/\gamma > 1, \ \ s_{\text{in}} \ll \sqrt{\gamma} \, a_s. \tag{22}$$

The limiting expressions (21)–(22) are plotted in Fig. 3(c), and agree well with the numerical solutions. This helps explain why the PT phase of the linear system affects the isolation functionality of the nonlinear system. Both phenomena are determined by the parameter μ/γ, with a critical point at $\mu/\gamma = 1$; the kink in the isolation ratio arises from switching steady-state solution branches at the critical point.

VI.   IMBALANCED INPUT/OUTPUT COUPLINGS

Thus far, we have assumed that the waveguide-resonator couplings, κ_1 and κ_2, are equal. If the couplings are unequal, the isolation behavior of the system can be quite different. To study this, we replace Eq. (9) with

$$\gamma_1 + \kappa_1 = \gamma_2 + \kappa_2 = 2\gamma. \tag{23}$$

For $g_0 = 4\gamma$, the gain in resonator 1 is

$$g = \frac{2\gamma}{1 + |a_1/a_s|^2} - \gamma, \tag{24}$$

which ensures that the decoupled system remains PT symmetric, as before, with critical point $\mu = \gamma$. With this generalization, the steady-state equations (14)–(16) are altered only by the replacements

$$\begin{aligned} \beta &\to \frac{\kappa_2}{\gamma}\beta \quad \text{(Forward)} \\ \beta &\to \frac{\kappa_1}{\gamma}\beta \quad \text{(Backward)}. \end{aligned} \tag{25}$$

By varying the couplings and losses so that Eq. (23) is satisfied, we can access different values of κ_1/κ_2, subject to the constraint $0 < \kappa_1, \kappa_2 < 2\gamma$.
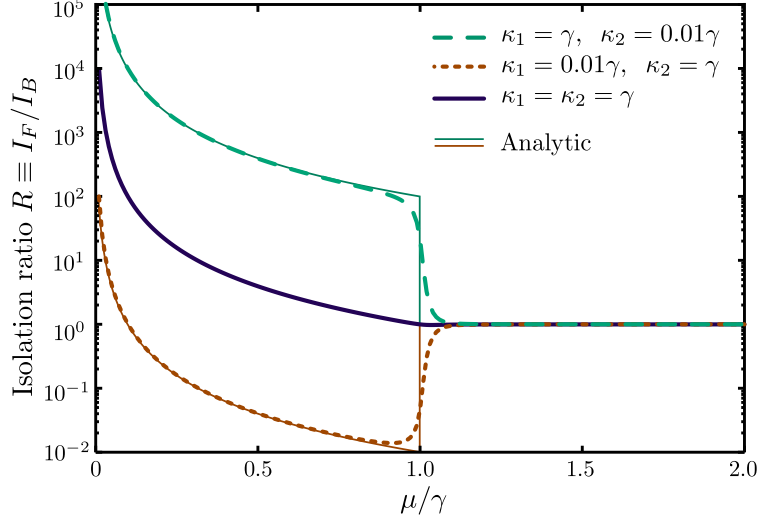
11

FIG. 4. Isolation ratio versus μ/γ for different microcavity-waveguide coupling strengths. The system parameters are $\Delta\omega = 0$, $s_{\text{in}} = 0.03$, $a_s = 3$, $\gamma = 1$, and $g_0 = 4\gamma$. Thin solid lines show the analytic approximation in the weak-input ($s_{\text{in}} \ll \sqrt{\gamma}\, a_s$) limit, given by Eq. (26).

The discussion of Section V generalizes to this case in a straightforward way. Using the previous zero-detuning and weak-input assumptions, we find that $x_F/x_B \approx 1$ for $\mu/\gamma < 1$, as before; but for $\mu/\gamma > 1$, Eq. (25) gives $x_F/x_B \approx \beta_F/\beta_B = (\kappa_2/\kappa_1)(\mu/\gamma)^2$. The isolation ratio now becomes

$$
R = (\kappa_1/\kappa_2)(\mu/\gamma)^{-2} x_F/x_B
$$
$$
\approx \begin{cases} (\kappa_1/\kappa_2)\,(\mu/\gamma)^{-2} & \text{for } \mu/\gamma < 1 \\ 1 & \text{for } \mu/\gamma > 1. \end{cases} \tag{26}
$$

For $\kappa_1 \neq \kappa_2$, this predicts a discontinuity in the isolation ratio at $\mu/\gamma = 1$.

Fig. 4 plots the isolation ratios at zero detuning. The equal-coupling case, which we have previously discussed, is shown as a solid black curve. For comparison, we also plot the isolation ratio curves for $\kappa_1 \ll \kappa_2$, and for $\kappa_1 \gg \kappa_2$. In all three cases, the isolation ratio approaches unity for $\mu/\gamma > 1$. Below the critical value, however, the unequal-coupling curves change abruptly by a factor of κ_1/κ_2, in this case by two orders of magnitude. (Interestingly, for $\kappa_1 \ll \kappa_2$, the isolation ratio *decreases* below unity, before becoming large again for $\mu/\gamma \to 0$.) The numerical results match Eq. (26) very well.

This phenomenon may be exploited in device applications for realizing an actively switch-able optical isolator. Using a small variation in the controlling μ/γ parameter (e.g., by

12

varying the inter-cavity separation, which affects μ), we can switch between strong optically isolating and reciprocal regimes.

VII. CONCLUSION

We have analyzed the relationship between the linear and nonlinear behaviors of dual microcavity resonators with gain and loss. The PT transition of the linear system is shown to correspond closely with the dynamical and steady-state behaviors of the gain-saturated nonlinear system, for which PT symmetry does not strictly apply. For $\mu > \gamma$, corresponding to the linear system's "PT-symmetric" phase, the resonances are always asymptotically stable, and the isolation ratio approaches unity. But for $\mu < \gamma$, corresponding to the linear system's "PT-broken" phase, the coupled-mode dynamics are unstable at sufficiently large frequency detunings. For steady-state operation, it is thus preferable to adopt zero detuning.

Using the crucial "weak-input" approximation, Eq. (18), we derived a kink in the isolation ratio at the critical point $\mu = \gamma$. Upon relaxing the constraint of equal waveguide-port couplings, this kink turns into a discontinuity, meaning that the isolation ratios vary extremely quickly with μ/γ in the vicinity of the critical point. This could be useful for actively-controllable on-chip optical isolators.

APPENDIX A: STABILITY ANALYSIS

This appendix discusses the stability analysis for the nonlinear coupled-mode equations. For forward transmission, we combine Eqs. (1)–(3) and (9)–(11) with the "PT symmetry" condition $g_0 = 4\gamma$, to obtain the time-dependent equations

$$\frac{da_1}{dt} = \left(i\Delta\omega - \frac{\gamma + \kappa_1}{2} + \frac{2\gamma}{1 + |a_1/a_s|^2} \right) a_1(t) - i\mu a_2(t), \tag{A1}$$

$$\frac{da_2}{dt} = (i\Delta\omega - \frac{\gamma + \kappa_2}{2}) a_2(t) - i\mu a_1(t) + \sqrt{\kappa_2}\, s_{\text{in}}. \tag{A2}$$

We assume a steady-state input s_{in}, and define

$$a_1(t) = \tilde{a}_1 + \rho_1(t) \tag{A3}$$

$$a_2(t) = \tilde{a}_2 + \rho_2(t), \tag{A4}$$

where $\tilde{a}_{1,2}$ is the steady-state solution that we wish to analyze and $\rho_{1,2}(t)$ are time-dependent perturbations. We insert this into Eqs. (A1)–(A2), omitting terms that are quadratic or higher-order in ρ_1 and ρ_2. The gain-saturation factor simplifies to:

$$\frac{2\gamma}{1 + |a_s|^{-2}(\tilde{a}_1 + \rho_1)(\tilde{a}_1^* + \rho_1^*)} \approx \frac{2\gamma}{1 + |a_s|^{-2}(|\tilde{a}_1|^2 + \tilde{a}_1\rho_1^* + \tilde{a}_1^*\rho_1)} \tag{A5}$$

$$\approx \frac{2\gamma}{1 + |\tilde{a}_1/a_s|^2}\left[1 - \frac{\tilde{a}_1\rho_1^*(t) + \tilde{a}_1^*\rho_1(t)}{|a_s|^2 + |\tilde{a}_1|^2}\right]. \tag{A6}$$

The result is a pair of time-dependent equations,

$$\frac{d\rho_1}{dt} = A\rho_1(t) + B\rho_1^*(t) + C\rho_2(t) \tag{A7}$$

$$\frac{d\rho_2}{dt} = C\rho_1(t) + D\rho_2(t), \tag{A8}$$

where

$$A = i\Delta\omega - \frac{\gamma + \kappa_1}{2} + \frac{2\gamma}{1 + |\tilde{a}_1/a_s|^2} - \frac{2\gamma|\tilde{a}_1/a_s|^2}{(1 + |\tilde{a}_1/a_s|^2)^2} \tag{A9}$$

$$B = -\frac{2\gamma\,\tilde{a}_1^2/|a_s|^2}{(1 + |\tilde{a}_1/a_s|^2)^2} \tag{A10}$$

$$C = -i\mu \tag{A11}$$

$$D = i\Delta\omega - \frac{\gamma + \kappa_2}{2} \tag{A12}$$

We then assume that the perturbations have the exponential time-dependence

$$\rho_1(t) = u_1 e^{\lambda t} + v_1^* e^{\lambda^* t} \tag{A13}$$

$$\rho_2(t) = u_2 e^{\lambda t} + v_2^* e^{\lambda^* t}. \tag{A14}$$

Plugging these into Eqs. (A7)–(A12), we derive the matrix equation

$$\begin{bmatrix} A & B & C & 0 \\ B^* & A^* & 0 & C^* \\ C & 0 & D & 0 \\ 0 & C^* & 0 & D^* \end{bmatrix} \begin{bmatrix} u_1 \\ v_1 \\ u_2 \\ v_2 \end{bmatrix} = \lambda \begin{bmatrix} u_1 \\ v_1 \\ u_2 \\ v_2 \end{bmatrix}. \tag{A15}$$
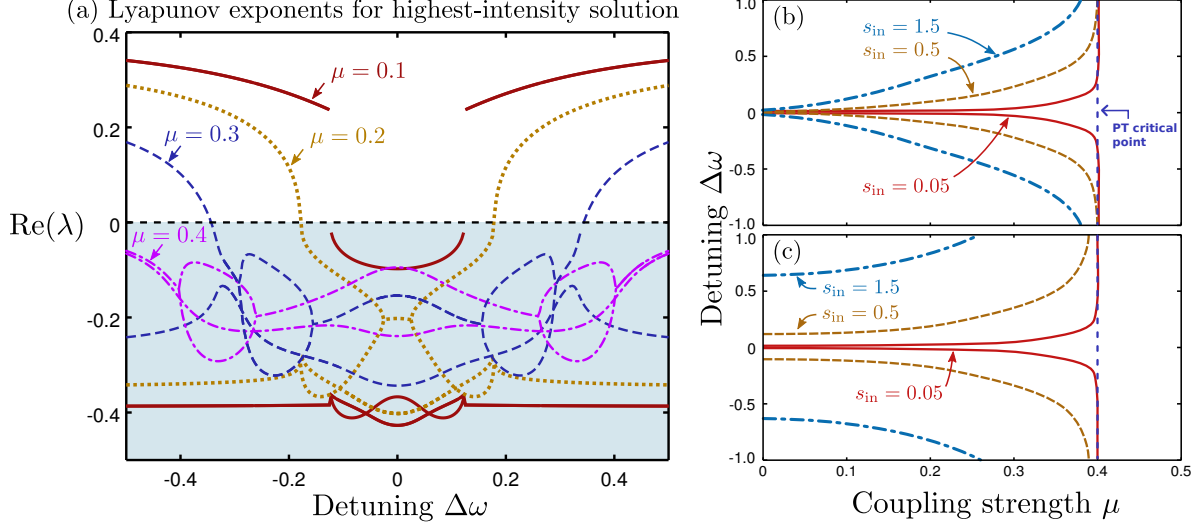
14

FIG. 5. (a) Lyapunov exponents for the highest-intensity steady-state solution under forward transmission, versus detuning $\Delta\omega$. Results are shown for $\mu \in \{0.1, 0.2, 0.3, 0.4\}$. The other model parameters are fixed at $\gamma = 0.4$ and $s_{\text{in}} = 0.5$. (b) Bounds of the asymptotic stability region under forward transmission, for several values of the amplitude s_{in}, with fixed $\gamma = 0.4$ and $a_s = 3$. The bandwidth of the asymptotic stability region increases with μ, and diverges at $\mu = \gamma$, which is the PT transition point of the linear system. (c) Bounds of the asymptotic stability region under backward transmission, with the same model parameters.

A stable state must have Lyapunov exponents $\text{Re}(\lambda) < 0$ for all four eigenvalues. For backward transmission, we can derive equations that have exactly the same form as Eqs. (A7)–(A15), except that the steady-state amplitudes $\tilde{a}_1$ and $\tilde{a}_2$ must be computed using Eqs. (4)–(5).

As discussed in Section IV, there is a domain in parameter space where the coupled-mode equations admit three physical steady-state solutions. By numerically computing the Lyapunov exponents, we find that the highest-intensity solutions are asymptotically stable. Fig. 5(a) plots the Lyapunov exponents for the highest-intensity solutions versus the detuning $\Delta\omega$ (in the parts of this plot that lie outside the three-solution domain, the highest-intensity solution is taken to be the single unique solution). It can be seen that the Lyapunov exponents become negative within a frequency band centered around $\Delta\omega = 0$. This agrees with Fig. 2(a)–(b). In particular, the discontinuity in the $\mu = 0.1$ curve is a result of crossing into the three-solution domain, whereupon a new branch of solutions,
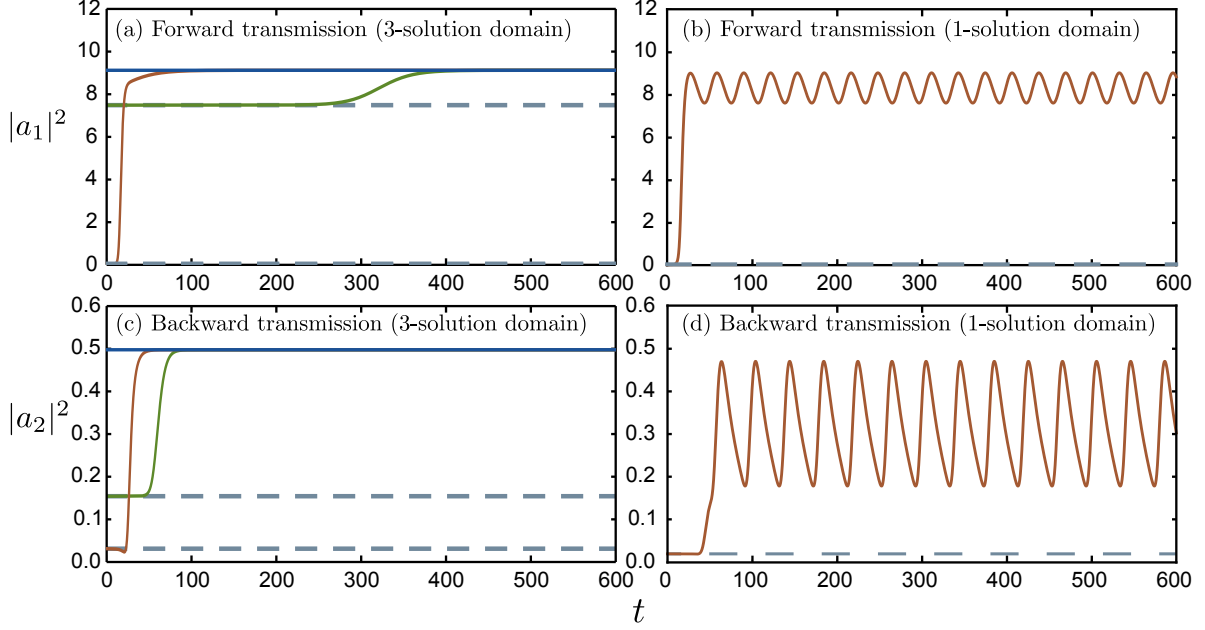
15

FIG. 6. Time-dependent mode amplitudes under (a) forward transmission for $\Delta\omega = 0$ (three-solution domain), (b) forward transmission for $\Delta\omega = 0.2$ (one-solution domain), (c) backward transmission for $\Delta\omega = 0$ (three-solution domain), and (d) backward transmission for $\Delta\omega = 0.2$ (one-solution domain). The other model parameters are $\mu = 0.1$, $a_s = 3.0$, and $s_{\mathrm{in}} = 0.5$. We start each simulation with initial conditions perturbed from a steady-state solution by $\delta a_1 = \delta a_2 = 0.001$. In the three-solution domain, perturbing the two lower-intensity solutions causes the system to evolve to the highest-intensity steady-state, which is asymptotically stable.

which are asymptotically-stable, become the highest-intensity solutions. For $\mu > \gamma$, which corresponds to the PT-symmetric phase of the linear system (Section III), the solution is asymptotically stable for all $\Delta\omega$.

As for the lower-intensity solutions within the three-solution domain, they are partially unstable, as one or more Lyapunov exponents satisfy $\mathrm{Re}(\lambda) > 0$.

To confirm these results, we solve the time-domain coupled-mode equations numerically (using the general-purpose ODE solver LSODE). Fig. 6(a) and (c) shows the time-dependent intensities, under forward and backward transmission, within the three-solution domain ($\mu = 0.1$ and $\Delta\omega = 0.0$, with $a_s = 3.0$ $s_{\mathrm{in}} = 0.5$ as before). The simulations show that perturbations to the lower-intensities steady states cause the system to evolve into the highest-intensity steady state, as expected from the stability analysis.

In the single-solution domain, the steady-state solution loses its asymptotic stability at
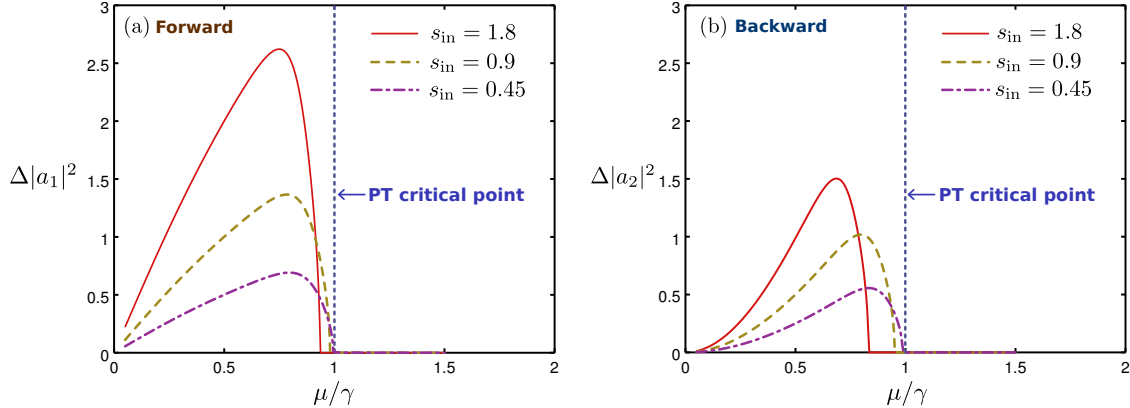
16

FIG. 7. Beating amplitudes $\Delta|a_{1,2}|^2$, defined as the difference of the maximum and minimum values of $|a_{1,2}(t)|^2$ over time t, versus the PT-breaking parameter μ/γ. The amplitudes $a_{1,2}(t)$ are solved numerically using the full time-dependent coupled-mode equations, using $\Delta\omega = 0.5$, $\gamma = 0.4$, $s_{\text{in}} = 0.5$, and $a_s = 3$.

large detunings, as indicated in Fig. 2(a)–(b). In this regime, small perturbations set up a self-sustained oscillation in the mode amplitudes, as shown in Fig. 6. The mid-point of this oscillation coincides with the real part of the "unphysical" complex root of Eq. (14) (which became unphysical at the boundary of asymptotic stability).

Fig. 7 shows the beating amplitude of $\Delta|a_1|^2$, versus μ/γ. The system is detuned so that $\Delta\omega = 0.5$. For small μ/γ, the beating is non-zero, but at $\mu \approx \gamma$ the system crosses the asymptotic stability boundary and reaches a steady state where $\Delta|a_1|^2 = 0$. This is yet another interesting link between the coupled-mode dynamics and the PT transition.

[1] M. Soljačić and J. D. Joannopoulos, Nature Mat. **3**, 211 (2004).

[2] J. Dirk *et al.*, Nature Phot. **7**, 8 (2013).

[3] H. Dotsch *et al.*, J. Opt. Soc. Am. B **22**, 240 (2005).

[4] M. Levy, J. Opt. Soc. Am. B **22**, 254 (2005).

[5] K. Gallo, G. Assanto, K. R. Parameswaran, and M. M. Fejer, Appl. Phys. Lett. **79**, 314 (2001).

[6] A. E. Miroshnichenko, E. Brasselet, and Y. S. Kivshar, Appl. Phys. Lett. **96**, 063302 (2010).

[7] M. Krause, H. Renner, and E. Brinkmeyer, Electron. Lett. **44**, 691 (2008).

[8] C. G. Poulton, R. Pant, A. Byrnes, S. Fan, M. J. Steel, and B. J. Eggleton, Opt. Ex. **20**,

21235 (2010).

[9] B. Peng, S. K. Özdemir, F. Lei, F. Monifi, M. Gianfreda, G. L. Long, S. Fan, F. Nori, C. M. Bender, and L. Yang, Nature Phys. **10**, 5 (2014).

[10] L. Chang, X. Jiang, S. Hua, C. Yang, J. Wen, L. Jiang, G. Li, G. Wang, and M. Xiao, Nature Phot. **8**, 7 (2014).

[11] R. El-Ganainy, K. G. Makris, D. N. Christodoulides, and Z. H. Musslimani, Opt. Lett. **32**, 2632–2634 (2007).

[12] K. G. Makris, R. El-Ganainy, D. N. Christodoulides, and Z. H. Musslimani, Phys. Rev. Lett. **100**, 103904 (2008).

[13] K. G. Makris, R. El-Ganainy, D. N. Christodoulides, and Z. H. Musslimani, Phys. Rev. A **81**, 063807 (2010).

[14] Z. H. Musslimani, K. G. Makris, R. El-Ganainy, and D. N. Christodoulides, Phys. Rev. Lett. **100**, 030402 (2008); J. Phys. **A** 41, 244019 (2008).

[15] A. Guo, G. J. Salamo, D. Duchesne, R. Morandotti, M. Volatier-Ravat, V. Aimez, G. A. Siviloglou, and D. N. Christodoulides, Phys. Rev. Lett. **103**, 093902 (2009).

[16] C. E. Rüter, K. G. Makris, R. El-Ganainy, D. N. Christodoulides, M. Segev, and D. Kip, Nat. Phys. **6**, 192 (2010).

[17] A. Regensburger, C. Bersch, M.-A. Miri, G. Onishchukov, D. N. Christodoulides, and U. Peschel, Nature **488**, 167 (2012).

[18] L. Feng *et al.*, Nature Mat. **12**, 108 (2013).

[19] S. Longhi, Phys. Rev. A **82**, 031801(R) (2010).

[20] Y. D. Chong, L. Ge, and A. D. Stone, Phys. Rev. Lett. **196**, 093902 (2011).

[21] C. M. Bender and S. Boettcher, Phys. Rev. Lett. **80**, 5243 (1998).

[22] C. M. Bender, M. V. Berry, and A. Mandilara, J. Phys. A **35**, L467 (2002).

[23] W. D. Heiss, J. Phys. A: Math. Theor. **45**, 444016 (2012).

[24] H. Ramezani, T. Kottos, V. Kovanis. and D. N. Christodoulides, Phys. Rev. A **85**, 013818 (2012).

[25] X.-Y. Lü, H. Jing, J.-Y. Ma, and Y. Wu, Phys. Rev. Lett. **114**, 253601 (2015).

[26] K. V. Kepesidis, T. J. Milburn, K. G. Makris, S. Rötter, and P. Rabl, arXiv:1508.00594 (2015).

[27] A. U. Hassan, H. Hodaei, M.-A. Miri, M. Khajavikhan, and D. N. Christodoulides, Phys. Rev. A **92**, 063807 (2015).

[28] H. A. Haus, *Waves and Fields in Optoelectronics* (Prentice-Hall, Englewood Cliffs, NJ, 1984).

[29] W. Suh, Z. Wang, and S. Fan, IEEE J. Quantum Elect. **40**, 1511 (2004).

[30] R. E. Hamam, A. Karalis, J. D. Joannopoulos, and M. Soljačić, Phys. Rev. A **75**, 053801 (2007).

[31] S. Zhang, D. A. Genov, Y. Wang, M. Liu, and X. Zhang, Phys. Rev. Lett. **101**, 047401 (2008).